



Constructing photocatalysis-self-Fenton system over a defective twin C₃N₄: In-situ producing H₂O₂ and mineralizing organic pollutants

Junpeng Yue^a, Hanpei Yang^{a,*}, Chen Liu^b, Qiang Zhang^a, Yanhui Ao^a

^a Key Laboratory of Integrated Regulation and Resource Development on Shallow Lakes, Ministry of Education, College of Environment, Hohai University, Nanjing 210098, China

^b Key Laboratory of Reservoir Aquatic Environment, Chongqing Institute of Green and Intelligent Technology, Chinese Academy of Sciences, Chongqing 400714, China

ARTICLE INFO

Keywords:

Defective twin carbon nitride
Photocatalysis-self-Fenton
Utilization of electrons
In-situ H₂O₂ production
Organic pollutants mineralization

ABSTRACT

A new strategy to realize efficient removal of organics from water through photo-self-Fenton was investigated. Characterizations and calculations demonstrated that a novel twin carbon nitride with abundant surficial N-defects and compressed π - π layer stacking can be constructed by thermal polymerization of urea under suitable basicity. Synergistically, the twins exhibited an in-situ H₂O₂ producing at a rate as high as 26.36 mM h⁻¹ g⁻¹ at 420 nm that exceeded most reported C₃N₄, and their mineralization rates for Tetracycline Hydrochloride, Bisphenol A, Ciprofloxacin, and Rhodamine B reached 8.8, 15.2, 9.1, and 13 times higher than that of pristine C₃N₄. It is concluded that enriching both of photogenerated electrons and molecular oxygens on specific sites plays a crucial role during photocatalysis-self-Fenton process. Particular attentions have to be paid to build structures achieving one and two-electron reduction of O₂, and activation of H₂O₂ to \bullet OH simultaneously.

1. Introduction

Photocatalysis based on semiconductors is widely expected to solve water environment pollution [1,2]. Unfortunately, photocatalytic mineralization of organic pollutants is still relatively inefficient. The essence of photocatalytic reaction is a chain reaction between reactive oxygen species (ROS) and organic pollutants. Obtaining high quantity and quality ROS is pivotal in improving photocatalytic efficiency [3,4]. Among recognized ROS (¹O₂, \bullet O₂, H₂O₂, and \bullet OH), H₂O₂ is the only molecule easily stored and plays an irreplaceable role in the photocatalysis-self-Fenton system. Numerous photocatalysts have been extensively explored for photocatalytic two-electron oxygen reduction reactions to produce H₂O₂ [5–8]. Especially carbon nitride (CN) has become a popular material due to its metal-free, certain light response capability, suitable energy band structure, and unique physicochemical properties [9,10]. However, the rapid recombination of electron-hole pairs and few exposed active sites limit the photoactivity of pristine CN [11,12].

Various strategies have been employed to modify pristine CN, such as metal/nonmetal dopant [13,14], morphologies modulation [15,16], noble metals loading [17–20], defects engineering [21,22], hybridization (with other semiconductors) [23–26]. Out of all these, defects

engineering is a common but effective method to obtain CN with excellent properties [27–29]. Many articles have shown that inducing structural defects can not only regulate the optical and electronic properties of CN, but also overcome kinetic frustration in the reduction of O₂, which effectively constructs a photocatalysis-self-Fenton system on the surface of CN [30,31]. Nonetheless, there are still the following issues that have not been taken seriously: (1) π - π layer stacking was always ignored in the design of carbon nitride with structural defects, which makes it challenging for charges transfer from bulk phase to surface; (2) In photocatalytic O₂-reduction reaction, remodeling defects to enhance the binding strength with O₂ may be more critical than simply exposing more defects; (3) It is necessary to take some measures to overcome the reverse recombination behavior of surface electrons. Therefore, obtaining a CN with functional defects on surface and compressed π - π layer stacking in bulk phase is worth exploring and challenging.

In this study, one-step thermal polymerization of urea in KOH-KCl was employed. KCl promoted the compression of π - π layer stacking and weakened the alkali-thermal reaction between KOH and CN. KOH caused the formation of highly crystalline nanoparticles on the surface and remodeled the original N-defects. A defective twin CN (KCN-0.5) was obtained. Compressed π - π layer stacking promoted the transfer of

* Correspondence to: Key Laboratory of Integrated Regulation and Resource Development on Shallow Lakes, Ministry of Education, Hohai University, Nanjing 210098, China.

E-mail address: yanghanpei@hhu.edu.cn (H. Yang).

<https://doi.org/10.1016/j.apcatb.2023.122716>

Received 7 December 2022; Received in revised form 5 March 2023; Accepted 31 March 2023

Available online 1 April 2023

0926-3373/© 2023 Elsevier B.V. All rights reserved.

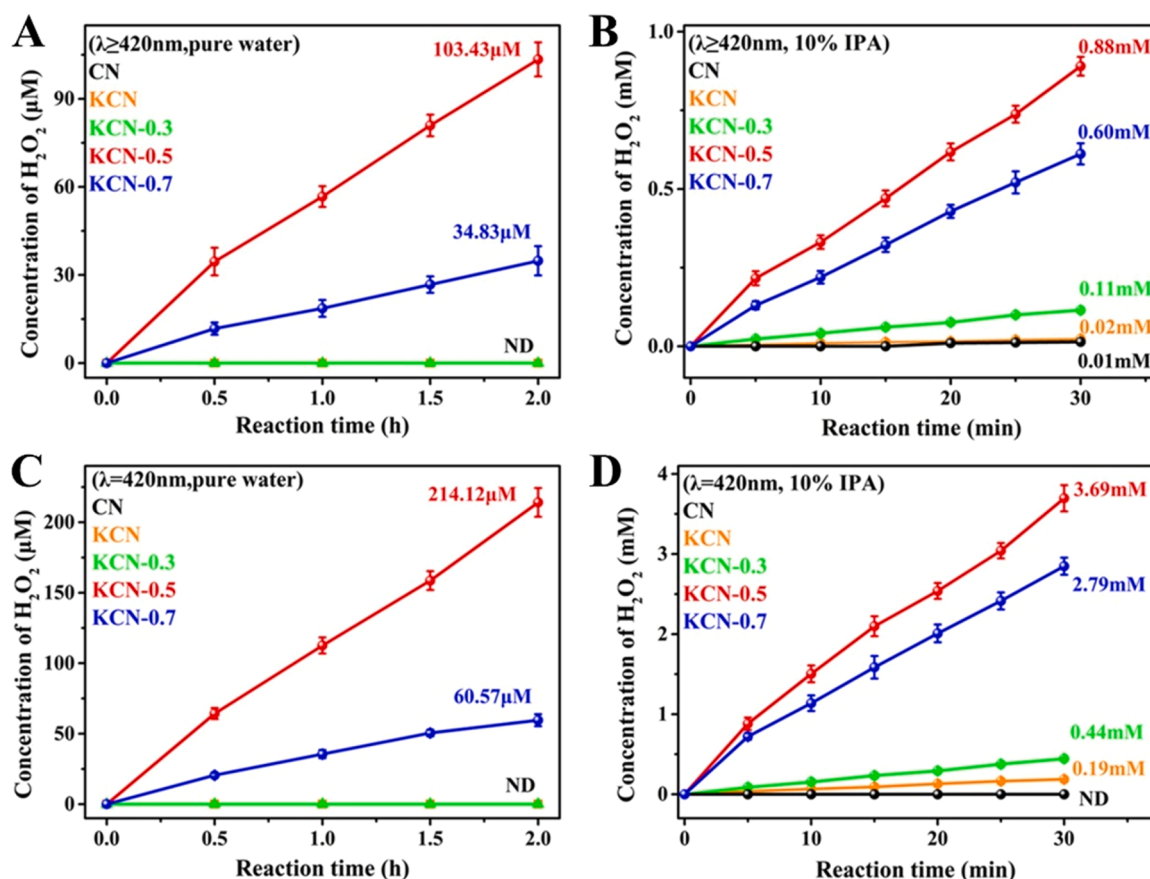


Fig. 1. (A-D) Time course of photocatalytic H₂O₂ production by as-prepared catalysts under different conditions.

charges from bulk phase to surface, twin structure separated the charges and limited the reverse recombination of electrons, and unique surface N-defects converged and transmitted electrons to O₂. Therefore, a photocatalysis-self-Fenton system has been successfully constructed over KCN-0.5. Compared to pristine CN, the rates of H₂O₂ production and organic pollutants purification over KCN-0.5 are significantly increased. This work provides a new idea for designing catalysts for solar energy conversion and environmental issues.

2. Experimental

2.1. Materials

Urea, Potassium hydroxide (KOH), Potassium chloride (KCl), Isopropyl alcohol (IPA), Sodium sulphate (Na₂SO₄), Potassium ferricyanide (K₃[Fe(CN)₆]), Potassium hexacyanoferrate (K₄Fe(CN)₆·3H₂O), Barium sulfate (BaSO₄), silver nitrate (AgNO₃), disodium hydrogen phosphate (Na₂HPO₄), sodium dihydrogen phosphate (NaH₂PO₄) and p-benzoquinone (BQ) were obtained from Sinopharm Chemical Reagent Co., Ltd. N, N-Diethyl-p-phenylenediamine sulfate (DPD) and peroxidase (POD) were obtained from Shanghai Aladdin Biochemical Technology Co., Ltd. Deionized water was obtained from a Millipore Milli-Q water purification system (Milford, MA, USA). All chemicals were used as received without further purification.

2.2. Synthesis

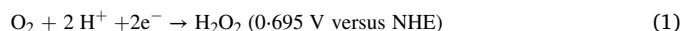
The catalysts were synthesized by a method of direct heating [32, 33]. First, 10 g urea, 10 g KCl, and a certain weight of KOH (0, 0.3, 0.5 and 0.7 g) were directly mixed and stirred in H₂O. Then the mixture was placed in a 50 mL sealed crucible wrapped with aluminized paper and

calcined at 550 °C under an air atmosphere for 4 h with a heating rate of 5 °C min⁻¹. After natural cooling, products were ground into powder and washed several times with deionized water (60 °C). Finally, dried the products at 60 °C for 24 h. The obtained products were KCN, KCN-0.3, KCN-0.5, and KCN-0.7 according to the amount of KOH.

For comparison, thermal polymerization of urea (10 g) in KOH (0, 0.5, and 0.7 g) obtained CN, CN-0.5, and CN-0.7, respectively.

2.3. Batch experiments

In the photocatalytic reaction, 25 mg as-prepared catalysts were dispersed in 50 mL of pure water or an aqueous solution containing 10 vol% isopropanol, ultrasound 1 min. A xenon lamp (CEL-HXF300, CEALIGHT, Beijing, China) as a light source. The inner wall radius of the reactor is 2.3 cm, and the reaction temperature was controlled at 25 °C by condensing unit. During the reaction, 3 mL of the mixture was collected every 5 min, centrifuged, the supernatant was taken, and filtrated with a 0.22 μm filtration membrane to remove the catalysts. The concentration of H₂O₂ was measured by the colorimetric method using DPD[4]. The standard curve is illustrated in Fig. S1. The specific process is as follows: 300 μL mixture solution of Na₂HPO₄ (0.01 M) and NaH₂PO₄ (0.09 M), 30 μL solution of DPD (10 mg/mL), and 30 μL solution of peroxidase (1 mg/mL) was added to deionized water (3 mL), successively. Then, added 1 mL of the filtrate to the mixed solution. Finally, the absorbance at 553 nm was measured by a UV-vis spectrometer to estimate the amount of H₂O₂ production. The photocatalytic ORR towards the production of H₂O₂ undergoes the following typical reaction process as below:



Therefore, the AQY was calculated as the following equation:

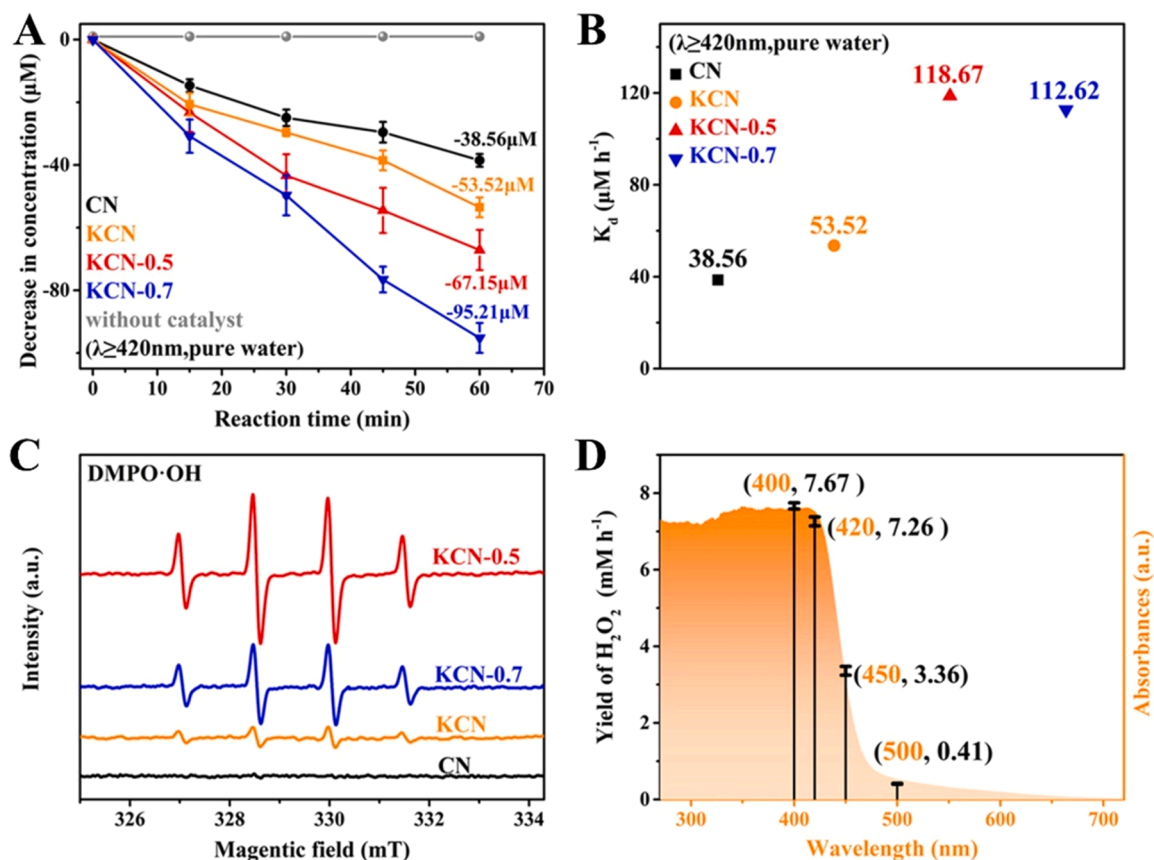


Fig. 2. (A) Photocatalytic H₂O₂ decomposition (1 μl, 30 wt% H₂O₂ solution, 50 mL water) by as-prepared catalysts (25 mg). (B) Rates of H₂O₂ decomposition by as-prepared catalysts (25 mg). (C) EPR signals of •OH over as-prepared catalysts. (D) Photocatalytic H₂O₂ production activity of KCN-0.5 (25 mg) with different monochromatic wavelengths.

$$AQY\% = N_{\text{(electrons)}} / N_{\text{(photons)}} = 2 \times N_{\text{(H}_2\text{O}_2)} / N_{\text{(photons)}} \times 100\% \quad (2)$$

Note: $N_{\text{(electrons)}}$, $N_{\text{(H}_2\text{O}_2)}$, and $N_{\text{(photons)}}$ refer to the total number of electrons transferred in the reaction, the molecular number of generated H₂O₂, and the number of incident photons in unit time, respectively.

Photocatalysis-self-Fenton mineralized tetracycline hydrochloride (TC), Bisphenol A (BPA), Ciprofloxacin (CIP), and Rhodamine B (RhB), were carried out under similar conditions.

2.4. Characterizations

Morphologies and high-angle annular dark-field scanning transmission electron microscopy (HAADF-STEM) acquired on a transmission electron microscope (TEM, FEI Talos F200X G2). X-ray diffraction (XRD) patterns were performed on a D8 ADVANCE X-ray diffractometer (Bruker, Germany) with Cu Kα radiation at $\lambda = 0.15406$ nm and 2θ range from 5.0° to 70° at the scanning rate of 7° min^{-1} . Fourier transform infrared (FTIR, Thermo NicoletIS50) investigated functional groups of the materials. Brunauer-Emmett-Teller (BET) surface area of materials was measured by a nitrogen adsorption device (Micromeritics ASAP 2460). Elemental compositions were obtained from an X-ray photoelectron spectrometer (XPS, PHI 5000 Versaprobe III) operated at 15 kV and 4.5 mA using Al Kα as an exciting source (1486.6 eV). UV-vis diffuse reflectance spectra (UV-vis DRS) of materials were tested by UV-vis spectrophotometer (SHIMADZU UV-2450) between 200 nm and 800 nm, and BaSO₄ was used as a reference standard. Electron paramagnetic resonance (EPR) signals were detected by the Electron Spin Resonance Spectrometer (JES-X320). Total organic carbon (TOC) was measured by a TOC analyzer (ELEMENTAR, vario, Germany). Photoluminescence

spectra were obtained from a FLS 1000 spectrophotometer (Edinburgh) with an excitation wavelength of 325 nm.

Electrochemical and photoelectrochemical analyses were performed by an electrochemical workstation (CHI660D) in a three-electrode setup. The Pt plate electrode was used as a counter electrode, Ag/AgCl electrode was used as the reference electrode, and fluorine-doped tin oxide (FTO) covered with different materials was used as a working electrode. In addition, transient photocurrent and Mott-Schottky curve measurements were performed with 0.5 M Na₂SO₄ as an electrolyte, electrochemical impedance spectroscopy (EIS) measurements were performed with 5 mM [Fe(CN)₆]^{3-/4-} and 0.1 M KCl mixed aqueous solution as electrolyte.

O₂ adsorption on materials was performed by temperature-programmed desorption (TPD, AutoChem II 2920). As-prepared catalysts (50 mg) were purged with helium (He) flow (30–50 mL/min) at 150 °C for one hour. After cooling to 50 °C, 10%O₂-He mixture (30–50 mL/min) was introduced for one hour and then switched to He s flow (30–50 mL/min) for one hour to remove the weakly physically adsorbed O₂ on the surface. Finally, tested the analytical measurement of O₂ in flowing He with a heating rate of $10^\circ \text{ C min}^{-1}$ until 500 °C.

2.5. Theoretical calculations

Gaussian 16 C.01, Multiwfn 3.8, ORCA 5.0.1, and VMD1.9.3 were employed for theoretical calculations and visualizations, and details are in [supporting information](#).

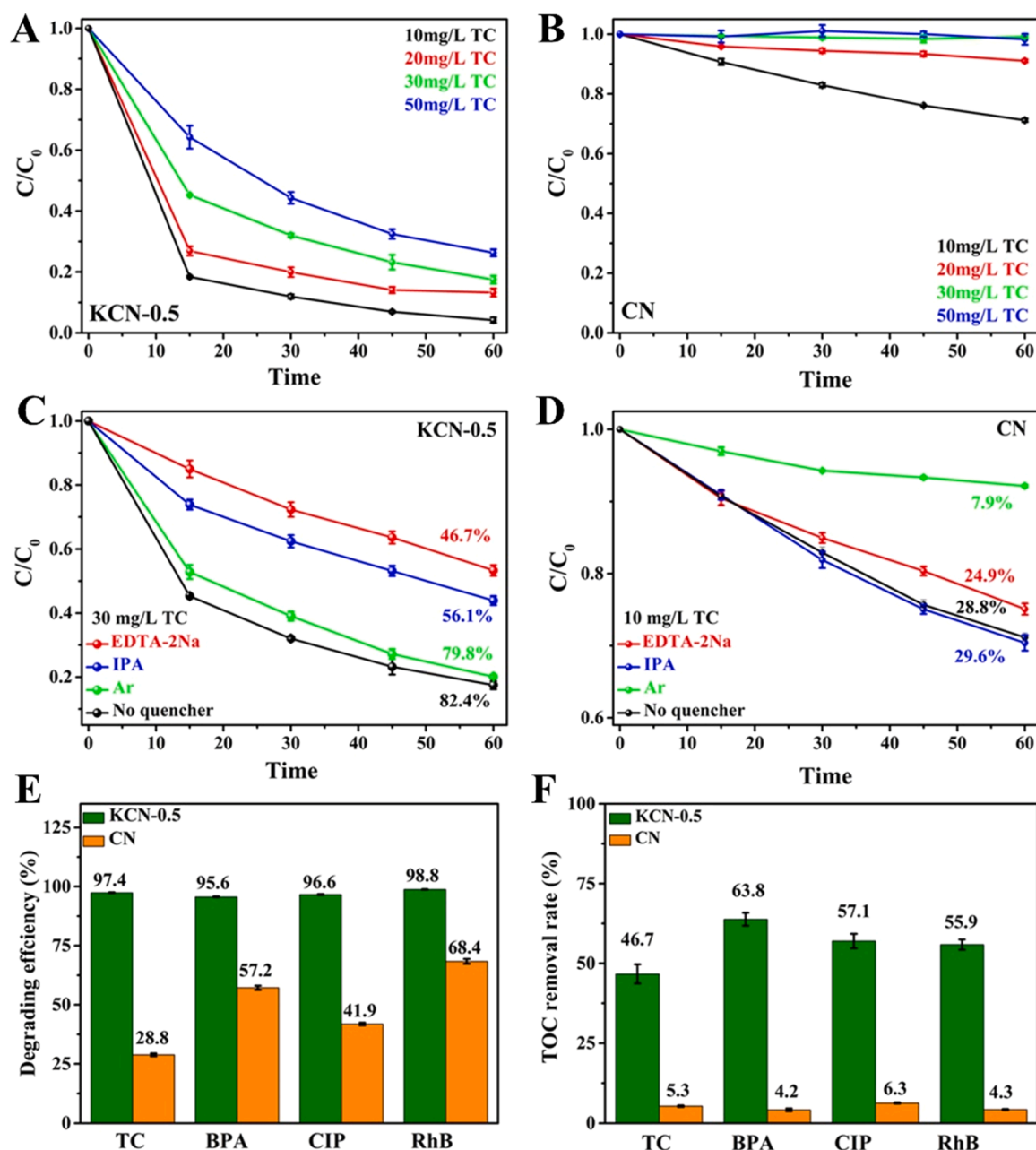


Fig. 3. (A, B) Degradation of TC (10–50 mg/L) on KCN-0.5 and CN ($\lambda \geq 420$ nm). (C, D) Results from capture experiments (EDTA-2Na for h^+ , IPA for $\bullet OH$, Ar for $\bullet O_2^-$, $\lambda \geq 420$ nm). (E, F) Degrading efficiencies and TOC removal rates of organic pollutants by KCN-0.5 and CN.

3. Results and discussions

3.1. Construction of a photocatalysis-self-Fenton system

In-situ production of H_2O_2 is a prerequisite for the construction of photocatalysis-self-Fenton systems. As recorded in Fig. 1 A (pure water, $\lambda \geq 420$ nm), no H_2O_2 was detected on CN, KCN, and KCN-0.3. The concentration of H_2O_2 detected on KCN-0.5 was $103.43 \mu M$ (2 h), and that of KCN-0.7 was $34.83 \mu M$ (2 h). In pure water, KCN-0.5 has better photocatalytic activity in producing H_2O_2 compared with other as-prepared catalysts. Adding isopropanol as a proton donor to further study the performance of as-prepared catalysts (Fig. 1B). Unsurprisingly, the H_2O_2 yield of all catalysts increased, and KCN-0.5 system afforded the highest rate of 1.76 mM h^{-1} , which is 88 times higher than that of CN system (0.02 mM h^{-1}). Unexpectedly, H_2O_2 concentration detected on KCN-0.5 and KCN-0.7 increased significantly after changing the light

illumination ($\lambda = 420$ nm), either in pure water (Fig. 1 C) or an aqueous solution containing IPA (Fig. 1D). According to the energy of a photon given by photoelectric effect equation: $E = hc/\lambda$ (E = energy of the photon, h = Planck's constant, c = speed of light, λ = wavelength). Under $\lambda \geq 420$ nm, there were more photons, which means more electrons were generated in the catalysts. For the reaction, there should be more two-electron reduction reaction of O_2 . But results obtained from the experiments were contrary, probably due to the further activation of H_2O_2 ($H_2O_2 + e^- \rightarrow \bullet OH + OH^-$).

For this, we tested the performances of as-prepared catalysts in activating H_2O_2 . As recorded in Fig. 2A, under light illumination ($\lambda \geq 420$ nm), there was no significant decrease in the concentration of H_2O_2 without any catalyst. After being decomposed by CN, KCN, KCN-0.5, and KCN-0.7, the concentration of H_2O_2 decreased by 38.56, 53.52, 67.15, and 95.21 μM , respectively. Combined with the production of H_2O_2 in pure water (Fig. 1A), the decomposition rates of H_2O_2 on

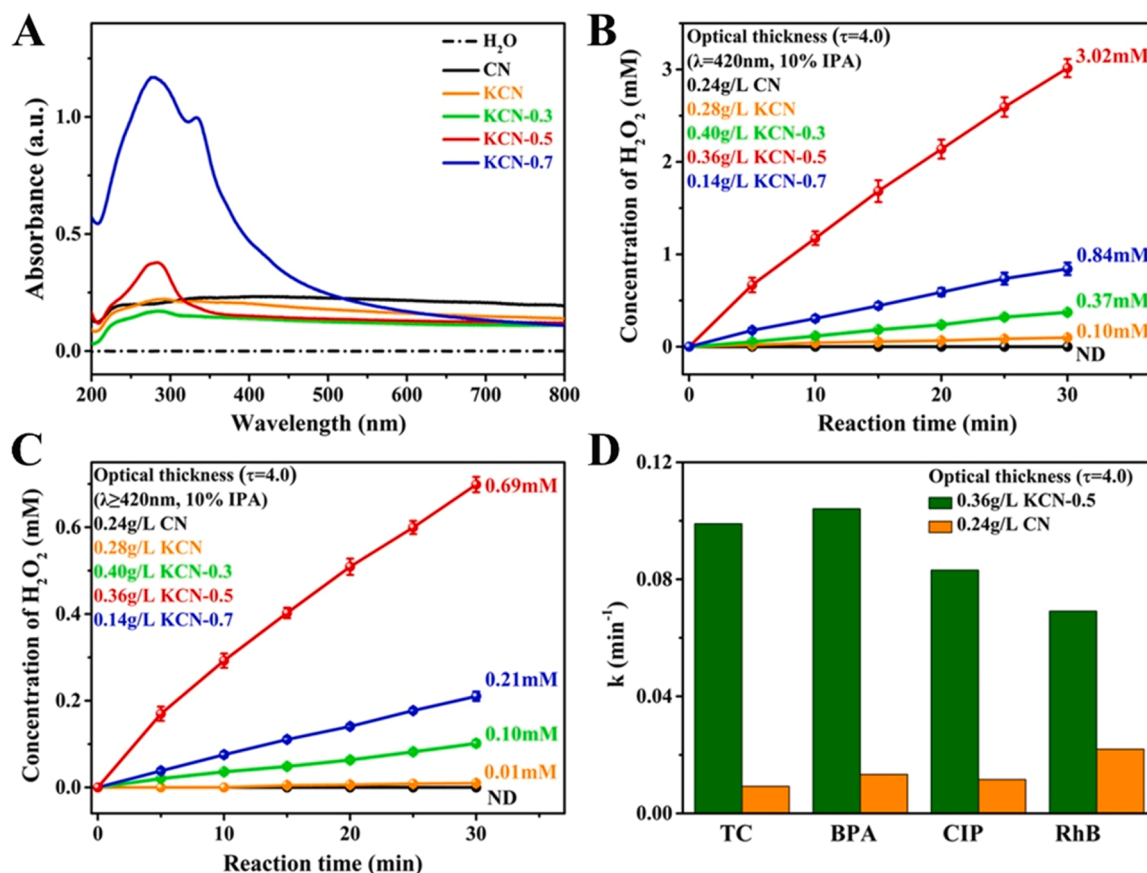


Fig. 4. (A) The absorbances of as-prepared catalysts in water suspension. At the same optical thickness ($\tau = 4.0$), (B-C) time course of photocatalytic H₂O₂ production for as-prepared catalysts under different conditions, (D) the degradation rate constants (k) of TC, BPA, CIP, and RhB by KCN-0.5 and CN ($\lambda \geq 420$ nm).

CN, KCN, KCN-0.5, and KCN-0.7 (25 mg) were 38.56, 53.52, 118.67, and 112.62 $\mu\text{mol h}^{-1}$ (Fig. 2B), respectively. KCN-0.5 can effectively construct a photocatalysis-self-Fenton system, further confirmed by EPR signals of DMPO- $\bullet\text{OH}$ spin-trapping in pure water. As recorded in Fig. 2C, KCN-0.5 generated a higher concentration of $\bullet\text{OH}$ than other catalysts. Besides, under a xenon lamp with 400, 420, 450, and 500 nm bandpass filter as the light source, the yield of H₂O₂ detected on KCN-0.5 reached 7.67, 7.26, 3.36, and 0.41 Mm/h, respectively (Fig. 2D). These show KCN-0.5 can effectively produce H₂O₂ at different wavelengths, providing evidence that the decrease under $\lambda \geq 420$ nm is due to the further activation of H₂O₂.

3.2. Removal of organic pollutants through photocatalysis-self-Fenton reaction

Firstly, 10 mg KCN-0.5 or CN were dispersed in a Tetracycline Hydrochloride (TC) solution (50 mL) for photocatalytic reaction. As recorded in Fig. 3A, KCN-0.5 showed excellent performance in the photocatalytic degradation of TC. Even if the concentration of TC reached 50 mg/L, the light-absorbance of TC in the KCN-0.5 system at 360 nm decreased significantly. In contrast, the photocatalytic degradation performance of CN was poor (Fig. 3B). The quenching experiments (Fig. 3C-D) indicated that the active species in their systems were different. In the degradation of TC, the main active species in KCN-0.5 system were $\bullet\text{OH}$ and h^+ , while that was $\bullet\text{O}_2^-$ in CN system. Furthermore, we tested the photocatalytic degradation and mineralization of KCN-0.5 for multiple organic pollutants. After an hour of reaction: TC, BPA, CIP, and RhB degradation efficiencies over KCN-0.5 were more than 95% (Fig. 3E), and the TOC removal rates of TC, BPA, CIP, and RhB by KCN-0.5 were 8.8, 15.2, 9.1, and 13 times higher than that by CN

(Fig. 3F). Obviously, KCN-0.5 can effectively degrade and mineralize organic pollutants through a photocatalysis-self-Fenton reaction.

3.3. Comparison of photocatalytic activity at the same optical thickness

The photon absorption rate of catalyst is one of the important factors affecting the photocatalytic activity, thus it is necessary to perform photocatalytic experiments at the same average photon absorption rate [34,35]. According to the Beer-Lambert law: $A = \log(1/T) = \epsilon bc$ (A , T , ϵ , b , and c refer to absorbance, transmittance, extinction coefficient, optical path length, and concentration of light absorbing substance, respectively) [36]. The average extinction coefficients of CN, KCN, KCN-0.5, and KCN-0.7 are calculated (The absorbances of as-prepared catalysts in aqueous suspension are depicted in Fig. 4A). ① $\lambda = 420$ nm, $\epsilon_1 = 5825, 4925, 3400, 3700, 10325$ cm²/g; ② $420 \leq \lambda \leq 460$ nm (The band gap of carbon nitride is ~ 2.7 eV, thus the longest absorbable incident wavelength is ~ 460 nm), $\epsilon_2 = 5780, 4795, 3320, 3596, 8959$ cm²/g. In experiments, the reactor was a cylinder with an inner wall radius of 2.3 cm, a liquid depth of 3.0 cm, and the optical thickness (τ) of the system was set to 4.0 [37]. According to the formula $\tau = hc\epsilon_a$ (h , C , and ϵ_a refer to the depth of liquid in system, catalyst concentration, and average extinction coefficient). Since the values of ϵ_1 and ϵ_2 are very close, the concentrations of CN, KCN, KCN-0.3, KCN-0.5, and KCN-0.7 were set to 0.24, 0.28, 0.40, 0.36, and 0.14 g/L. At the same optical thickness, KCN-0.5 showed excellent photocatalytic performance. The performance of KCN-0.5 was far more than that of other as-prepared catalysts in producing H₂O₂ (Fig. 4B-C), and the degradation rate constants (k) of TC, BPA, CIP, and RhB by KCN-0.5 were 10.6, 7.8, 7.2, and 3.2 times higher than that of CN (Fig. 4D).

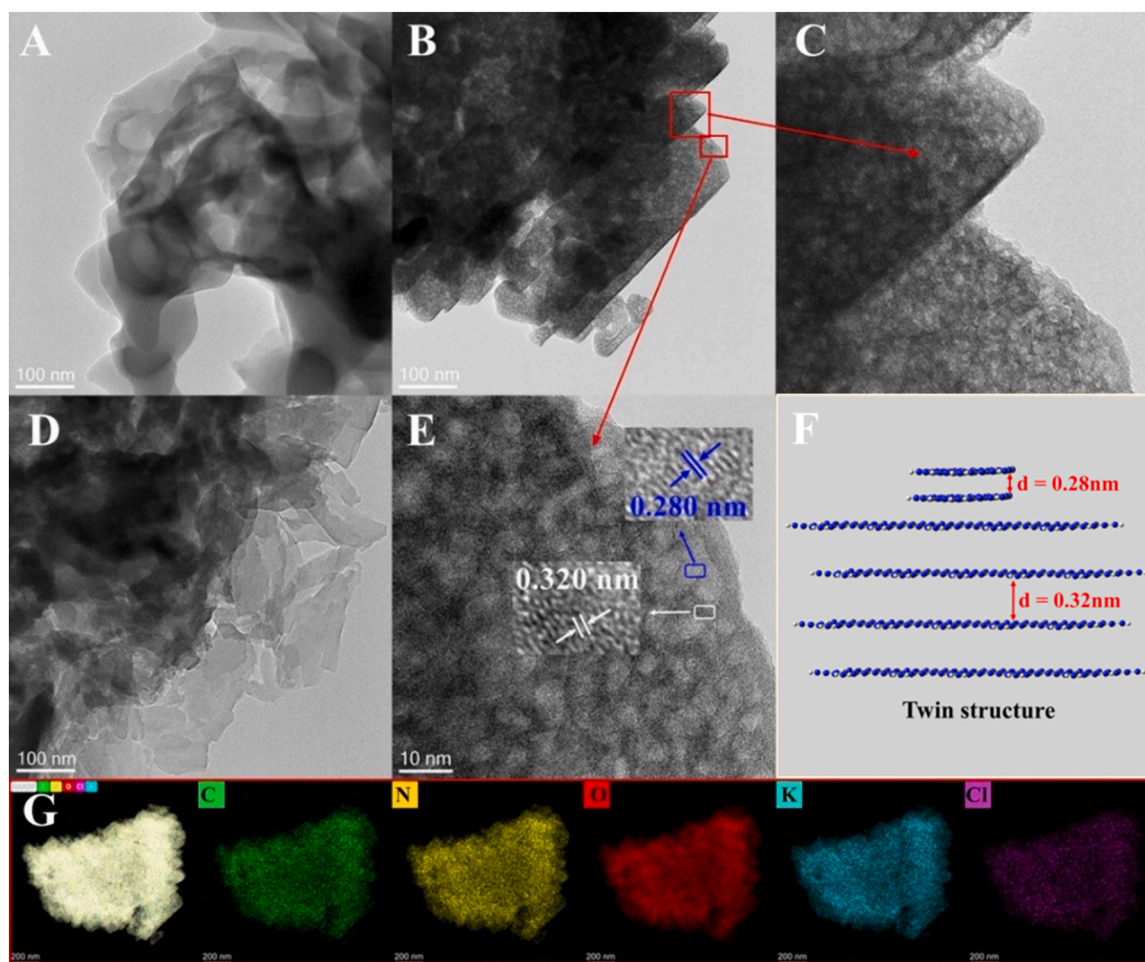


Fig. 5. TEM images of (A) KCN, (B-C) KCN-0.5, (D) KCN-0.7. (E) HR-TEM images of KCN-0.5. (F) Schematic diagram about twin structure. (G) Elemental (C, N, O, K, Cl) mappings in KCN-0.5.

3.4. Analysis of crystal structure and surface chemical composition

The morphologies of as-prepared catalysts were observed by transmission electron microscope. KCN prepared by thermal polymerization in KCl are nanosheets with a smooth surface (Fig. 5A). After the addition of KOH, the surface of KCN-0.5 are covered with nanoparticles (Fig. 5B-C), while KCN-0.7 are thinner in dimension but without nanoparticles on its surface (Fig. 5D). Further, KCN-0.5 was observed by high-resolution TEM (Fig. 5E), two different lattice fringes were recorded (Fig. S2, FFT patterns): Lattice spacing $d \approx 0.320$ nm of black-shaded correspond to the (002) plane of heptazine[38], that of the white part (nanoparticles) were $d \approx 0.280$ nm. Possibly because KOH etched the surface of CN, resulting in an enhancement of van der Waals force between heptazine and K[39,40], thereby promoting further compression of π - π layer stacking distance and forming higher crystalline nanoparticles. This different π - π layer stacking distance at surface and bulk phase constitutes a twin structure[41] (Fig. 5F). Moreover, the elemental mappings show that C, N, and K elements are uniformly distributed in KCN-0.5 (Fig. 5G, detailed data are collected in Table S1). The surface of KCN-0.5 contains a large amount of O element, probably from adsorbed O_2 or H_2O , and detected only trace amounts of Cl.

X-ray diffraction (XRD) was employed to figure out the changes in crystal structures. As depicted in Fig. 6A, (001) and (002) peaks of pristine CN are located at 12.9° and 27.3° . Compared with CN, (001) and (002) peaks of KCN- x ($x = 0-0.5$) shift to 7.9° and 27.6° , representing changes of functional groups in-plane and compression of π - π layer stacking in bulk phase, respectively[42,43]. The XRD pattern on

KCN-0.7 shows a split peak from the (002) plane and a weak peak intensity signal at 29.6° , indicating that the addition of KOH causes the formation of multiple crystalline CN[44,45]. Notably, no signal of other peaks was recorded in KCN-0.5, but two different lattice fringes were recorded in HR-TEM images of KCN-0.5. Therefore, we speculate that higher crystalline nanoparticles are limited to the region of KCN-0.5 shallow surface and covered by signal of (002) peaks, so no obvious signal was recorded. Further, the FWHM of (002) peaks for CN, KCN, KCN-0.3, KCN-0.5, and KCN-0.7 are 0.81, 0.47, 0.46, 0.42, and 0.53. According to the Scherrer formula ($d = 0.9\lambda/(\beta\cos\theta)$), the crystallite sizes of CN, KCN, KCN-0.3, KCN-0.5, and KCN-0.7 are calculated to be approximately 10.09, 17.72, 17.79, 19.48, and 15.44 nm.

Fourier Transform Infrared (FTIR) spectra of as-prepared catalysts are depicted in Fig. 6B. KCN has been recorded as an extremely strong intensity for the asymmetric stretching peaks of cyano group ($-C\equiv N$) at 2180 cm^{-1} [46], showing a large number of N-defects are formed on the surface of KCN, this is because the thermal polymerization in KCl accelerated the deamination process[47,48]. After the addition of KOH, surface functional groups of KCN-0.5 changed again, mainly in two locations: the intensity of symmetric and asymmetric vibration peaks at 995 cm^{-1} increased, and N-H stretching peaks between 3000 and 3300 cm^{-1} disappeared[49,50]. Interestingly, with further usage of KOH (KCN-0.7), the intensities of $K-NC_2$ at 995 cm^{-1} and $-C\equiv N$ at 2180 cm^{-1} decreased, while the N-H stretching peak between 3000 and 3300 cm^{-1} reappeared.

X-ray electron spectroscopy (XPS) further analyzed the surface elemental composition and chemical states. N/C ratios of KCN, KCN-0.5,

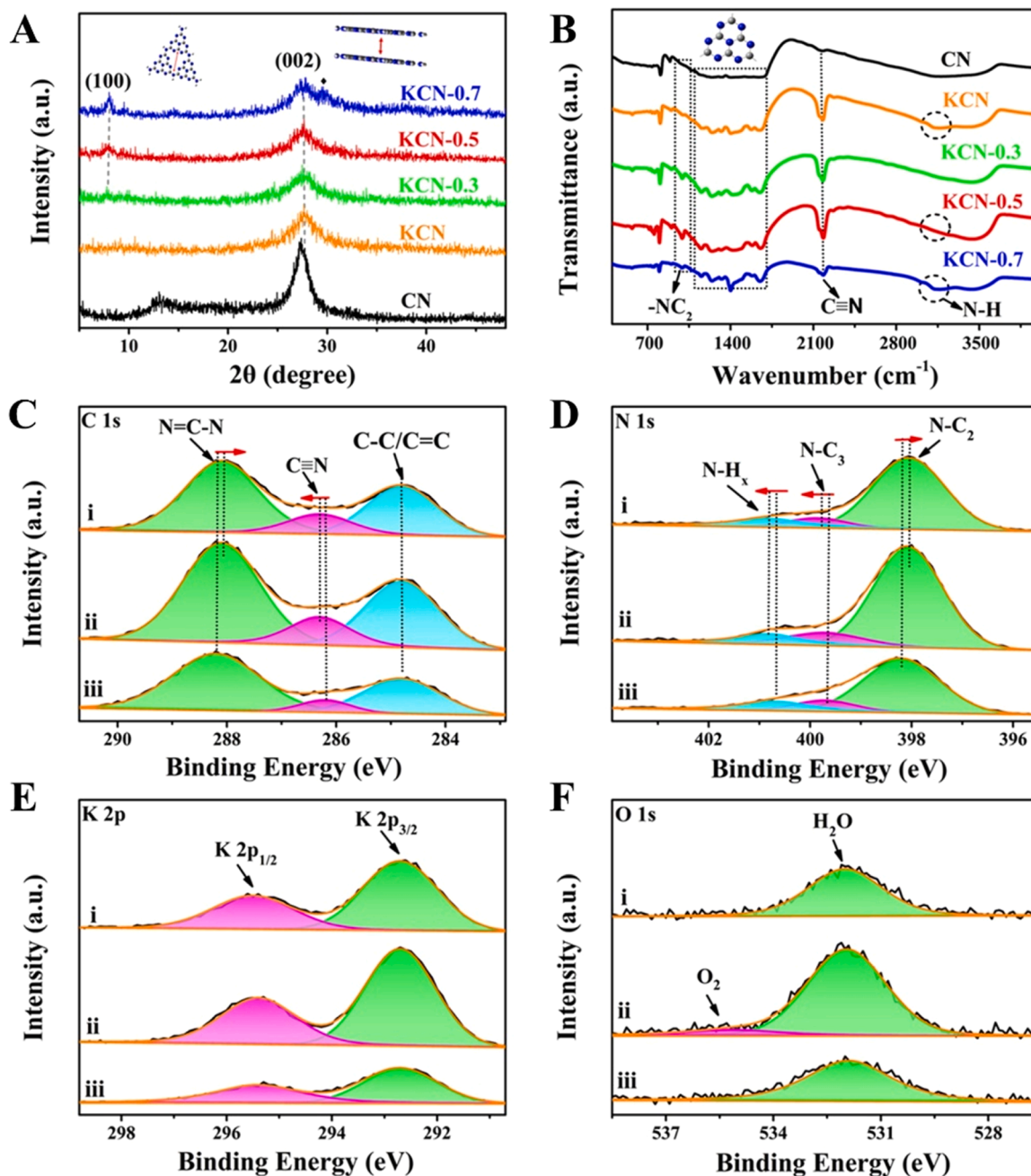


Fig. 6. (A) XRD patterns and (B) FTIR spectra on as-prepared catalysts. The high resolution XPS spectra of (C) C1s, (D) N1s, (E) K2p, and (F) O1s on as-prepared catalysts ((i) KCN-0.7, (ii) KCN-0.5, (iii) KCN).

and KCN-0.7 are 0.976, 0.878, and 0.936 (Table S2)). KOH changes the content of element N on the surface. Narrow scan C1s and N1s XPS peaks obtained from KCN, KCN-0.5, and KCN-0.7 were collected and deconvoluted to get more information. As indicated in Fig. 6 C-D, both the XPS peaks from C1s and N1s can be deconvoluted into three components[51, 52]. Detailed binding energy positions are statistically shown in Table S3. The binding energies of C1s and N1s from KCN-0.5 shift significantly compared with those from KCN, demonstrating electron densities of the heptazine chain on their surfaces have changed[53,54]. According to the proportion of N-containing components from KCN, KCN-0.5, and KCN-0.7 (Table S3), the N-H_x group is responsible for these changes, which was consistent with the changes observed in FTIR. Incidentally, the intercalation of K was confirmed by a specific characteristic peak of K-N (Fig. 6E) located at 292.7 eV[55]. Some element O (Fig. 6 F) and no element Cl (Fig. S3, Table S2) were detected on the

surface of KCN-0.5.

Summarizing the results from TEM, XRD, FTIR, and XPS, we speculate the formation process of as-prepared catalysts (Fig. 7 A). Consistent with other articles[40,56], KCN obtained through thermal polymerization of urea in KCl has a smooth surface and is rich in a common N-defect. KCN and KCN-x ($x = 0.3-0.7$) powders are yellow (Fig. S4A-D). While a strong etching reaction occurs during the thermal polymerization of urea only in KOH (0.5, 0.7 g), and the resulting products (CN-0.5, CN-0.7) were black (Fig. S4E-F). This indicates that KCl weakened the alkaline thermal reactions between KOH and CN. Therefore, there are abundant nanoparticles on the surface of KCN-0.5. KOH also removed the -NH_2 group, leading to a new N-defect in the nanoparticles. This new N-defect caused an enhancement of Van der Waals force between K and π - π layer, promoting further compression of π - π layer stacking distance in the nanoparticles. As a result, a defective

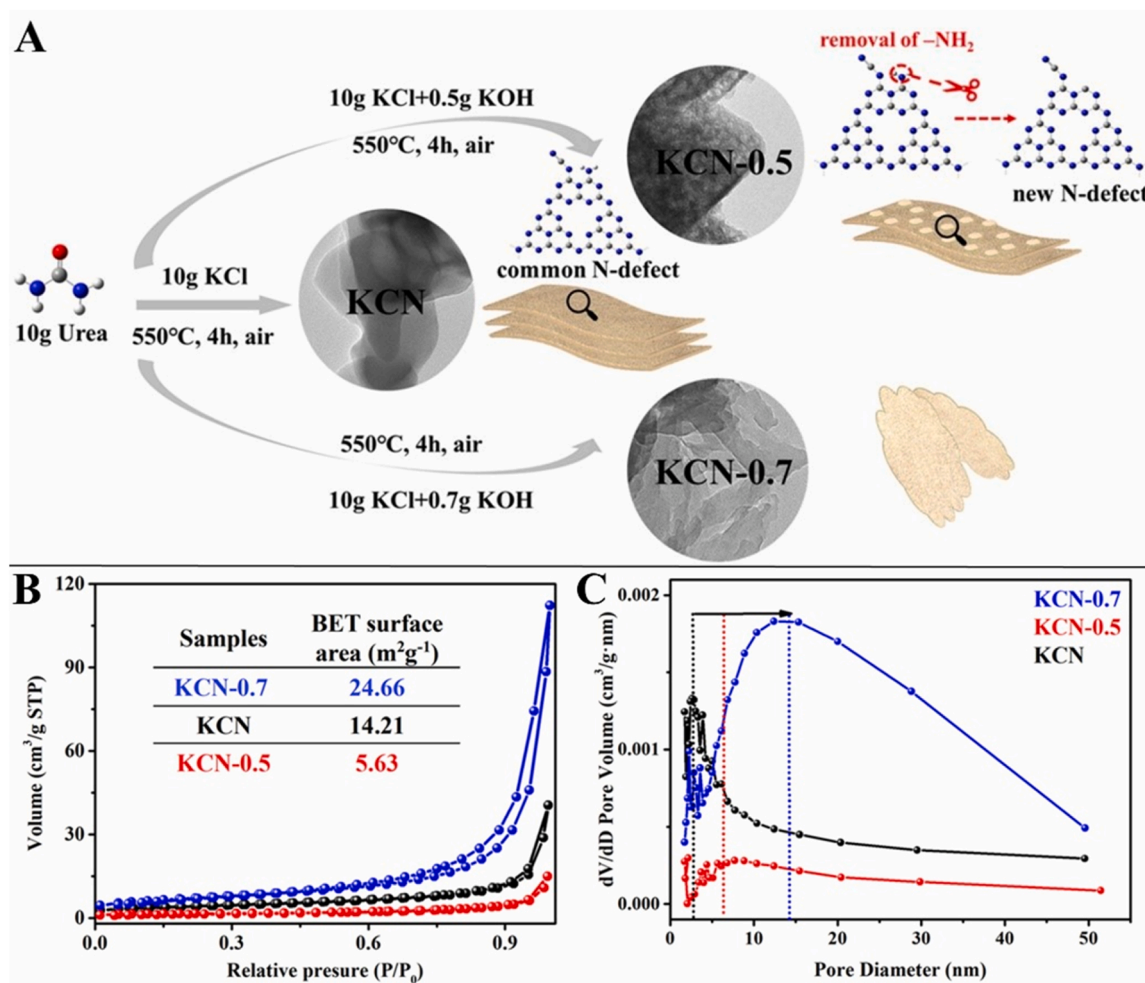


Fig. 7. (A) Schematic diagram about the formation process of as-prepared catalysts. (B) Nitrogen adsorption/desorption isotherms, BET surface areas, and (C) Pore size distributions of KCN, KCN-0.5, and KCN-0.7.

twin CN was obtained (KCN-0.5). Because excessive usage of KOH triggered the exfoliation of CN layer by layer, KCN-0.7 is thinner in dimension and without nanoparticles on its surface. Results from Brunauer Emmett Teller (BET) tests also provide indirect evidence for these. KCN, KCN-0.5, and KCN-0.7 exhibit typical Type-IV isotherms with H3-type hysteresis loops (Fig. 7B)[56,57], and BET surface areas are 14.21, 5.63, and $24.66 \text{ m}^2\cdot\text{g}^{-1}$, respectively (Inset in Fig. 7B). Estimated from the BJH method, the pore distribution peaks of KCN, KCN-0.5, and KCN-0.7 are centered at approximately 2.72, 4.32, and 14.28 nm (Fig. 7C). Since no obvious pore was observed in TEM images (Fig. 5), these results are owing to the stacked pore of the materials. The compression of π - π stacking results in the smallest BET surface area and the fewest pore volume for KCN-0.5, while those of KCN-0.7 are the largest due to excessive etching.

3.5. Improved optical and electronic properties

The optical and electronic properties of catalysts are essential for constructing a photocatalysis-self-Fenton system. UV-vis diffuse reflectance spectra (DRS) of as-prepared catalysts are present in Fig. 8A. Compared with CN, subtle enhancements of $\pi \rightarrow \pi^*$ and $n \rightarrow \pi^*$ electronic transition were observed in KCN, which can be attributed to compressed π - π layer stacking and the N-defect[27,58], respectively. A further enhancement of electronic transition was observed in KCN-0.5 due to additional compression of π - π layer stacking and the new N-defect on surface nanoparticles. While exfoliation of surface nanoparticles and

re-exposure of $-\text{NH}_2$ resulted in a weakening of electron transition observed in KCN-0.7. The twin structure is also beneficial to improve the mobility of charge, as evidenced by strong transient photocurrent response (Fig. 8B), small EIS radius (Fig. 8C), and weak fluorescence signal (Fig. S5). Composed π - π layer stacking in bulk phase ensures the transfer of charge from bulk phase to surface, and K provides a channel for this[59]. Higher crystalline nanoparticles on the surface promote the separation of charges and inhibit the reverse recombination of electrons. What is more, density functional theory calculations were performed for the surface N-defect structures of KCN and KCN-0.5, respectively. As indicated in the density of states (Fig. 8D-E), after the removal of the $-\text{NH}_2$ group, the β -LUMO energy level of KCN-0.5 (-3.92 eV) is lower than that of KCN (-2.45 eV), and HOMO-LUMO gap of KCN-0.5 (2.79 eV) is smaller than that of KCN (4.18 eV). Meaning electron affinity of nanoparticles on the surface of KCN-0.5 is stronger, electrons transferred from the bulk phase will concentrate on the nanoparticles, further verify the excellent properties of KCN-0.5 in separating charges, and this is strongly supported by the shorter average lifetimes of charge carriers (Fig. 8F).

3.6. Properties of the new N-defect in adsorbing and reducing O_2

Temperature-programmed desorption of O_2 was employed to analyze the ability of the new N-defect to adsorb O_2 . As illustrated in Fig. 9A, the area and temperature of O_2 desorption peak on KCN-0.5 are more extensive than that of KCN, representing the new N-defect on KCN-

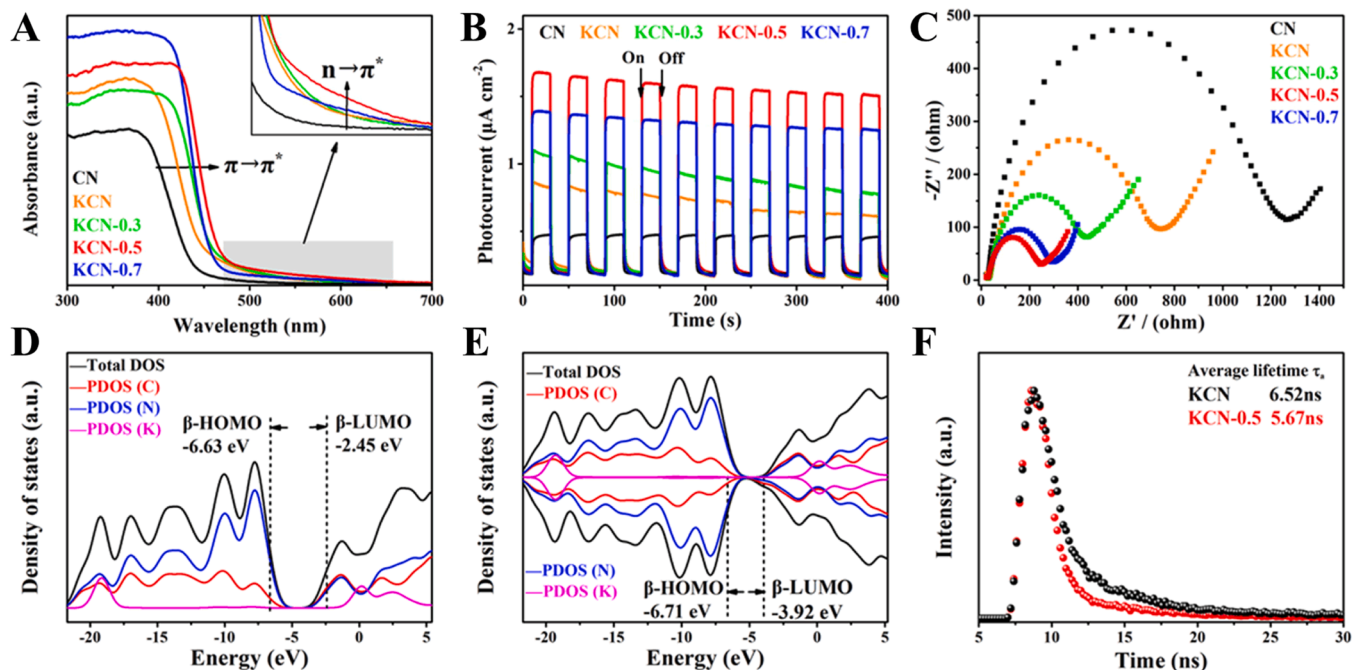


Fig. 8. (A) UV-vis DRS absorption spectra, (B) Transient photocurrent response and (C) EIS Nyquist plots performed on as-prepared catalysts. Total DOS and PDOS of (D) KCN and (E) KCN-0.5. (F) TRPL spectra recorded on KCN and KCN-0.5.

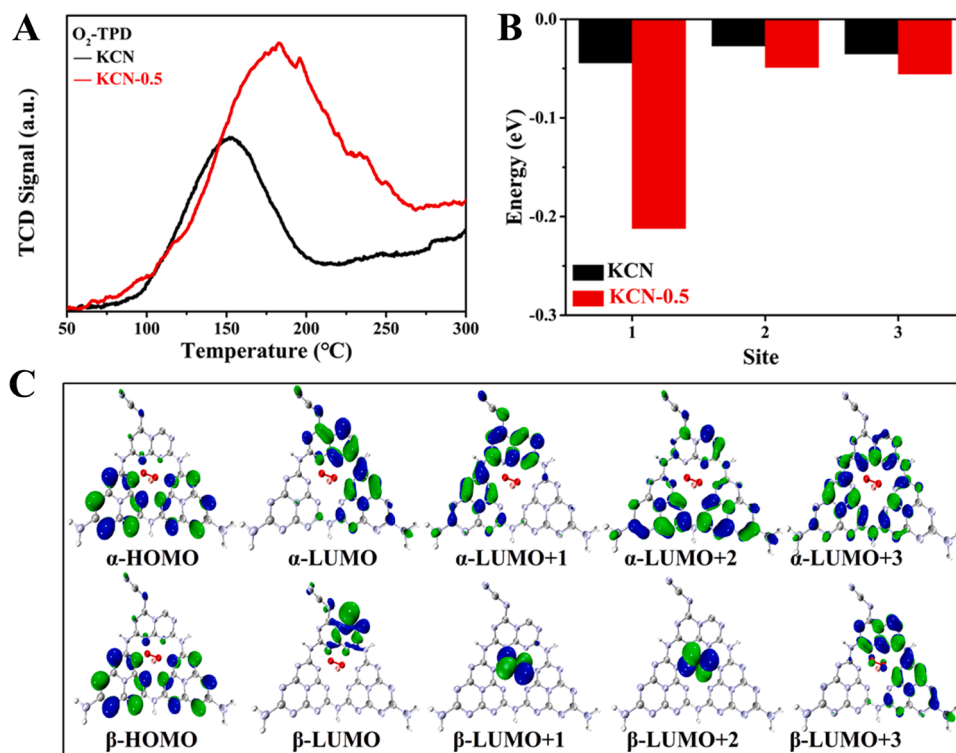


Fig. 9. (A) O_2 -TPD profiles of KCN and KCN-0.5. (B) E_{ads} of KCN and KCN-0.5 adsorbed O_2 at different positions. (C) Electronic structure of the optimized HOMO and LUMO of KCN-0.5 (The isosurface value is $0.03 \text{ e} \text{ \AA}^{-3}$. Green and blue isosurfaces represent electron and hole distributions, respectively).

0.5 can adsorb more O_2 and has stronger binding strength with O_2 . Pore volume and BET surface area of KCN-0.5 are the smallest (Fig. 7B-C), indicating this enhanced O_2 adsorption and binding performance of KCN-0.5 were caused by the new N-defect rather than the exposure of more N-defect sites. This new N-defect will help overcome the kinetic frustration for the reduction of O_2 [46], strongly supported by theoretical

calculations (Fig. 9B). The energy difference of the new N-defect (KCN-0.5) before and after adsorb O_2 is smaller than that of the common N-defect (KCN). Especially at the site where $-NH_2$ was removed (Site 1, Fig. S6), the energy difference reaches -0.212 eV , indicating removal of the $-NH_2$ is easier to adsorb O_2 and has a strong binding strength with O_2 . Therefore, kinetic frustration for reducing O_2 on the new N-defect

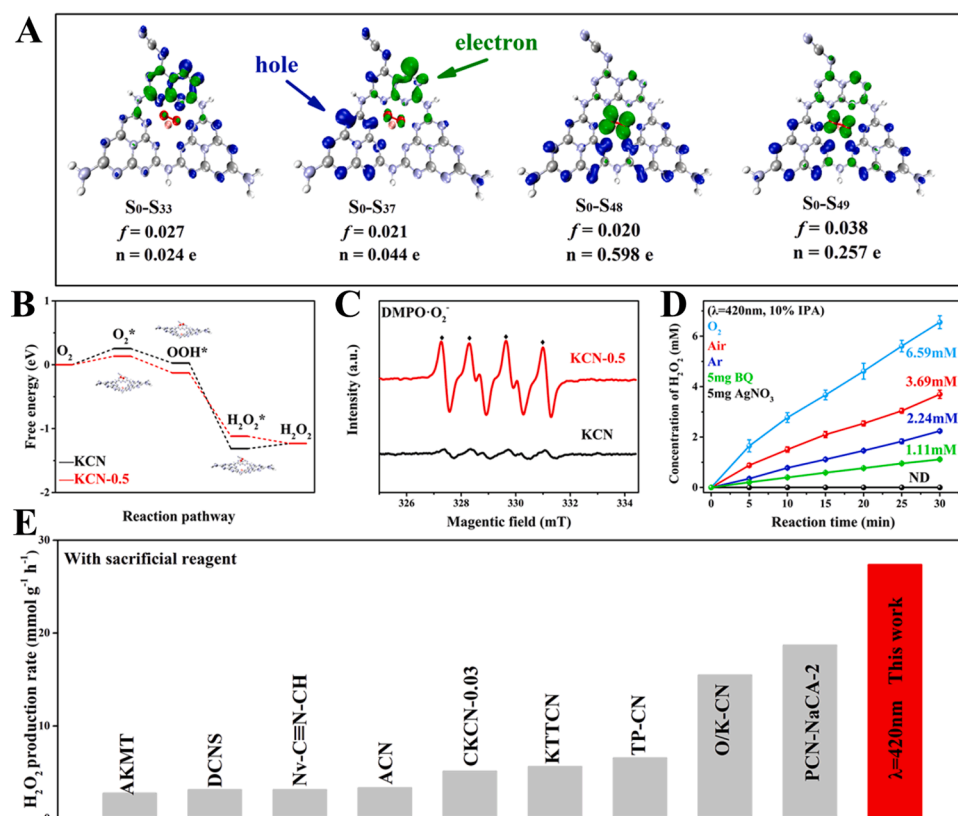


Fig. 10. (A) Electron-hole distribution on O_2 -adsorbed KCN-0.5 in different excited states (green isosurface: electron distribution, blue isosurface: hole distribution, the isosurface value is $0.03 e \text{ \AA}^{-3}$). (B) Free energy diagrams of ORR steps on KCN and KCN-0.5. (C) EPR signals of $\bullet O_2^-$ over KCN and KCN-0.5. (D) Time course of photocatalytic H_2O_2 production by KCN-0.5 under different condition ($\lambda = 420$ nm, 10% IPA). (E) Comparison for H_2O_2 production performance of KCN-0.5 and other CN-based catalysts.

has been reduced, allowing electrons to more easily transfer from the β spin-orbital of KCN-0.5 to the π^* orbital of O_2 (Fig. 9 C).

Moreover, the new N-defect endows the β spin-orbital of KCN-0.5 (Fig. 10 A) with a higher orbital contribution to the excited state than the N-defect of KCN (Fig. S7). Electrons in KCN-0.5 are mainly

concentrated at the new N-defect. In contrast, the electron distribution in KCN is disorderly. More electrons transmit directly from β spin-orbital of KCN-0.5 to the π^* orbital of O_2 in each excitation[60]. Therefore, the thermodynamic processes of photocatalytic $2e^-$ ORR on KCN-0.5 are smoother (Fig. 10B) than that on KCN. EPR signals of DMPO- $\bullet O_2^-$

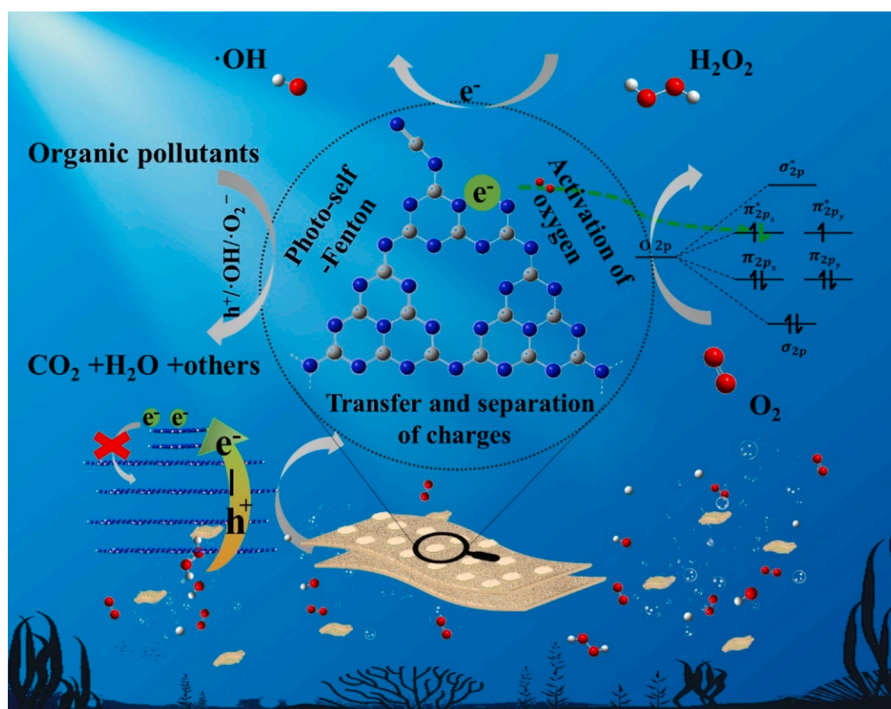


Fig. 11. Schematic illustration of photo-self-Fenton microenvironment on the surface of KCN-0.5. (Gray, blue, red, and white spheres represent C, N, O, and H atoms, respectively.).

spin-trapping, capture experiments, and photocatalytic oxygen reduction reactions in different atmospheres also verify this point. As recorded in Fig. 10 C, KCN-0.5 exhibited powerful signals compared with KCN, proving that the new N-defect of KCN-0.5 is more efficient in transferring photogenerated electrons to O_2 , thus accelerating the production of H_2O_2 . From the results of capture experiments (Fig. 10 D), the addition of $AgNO_3$ (e^- scavenger) completely inhibited the reaction, and the addition of 1,4-Benzoquinone ($\bullet O_2^-$ scavenger) largely prohibited the production of H_2O_2 (fell by 69.7%), these results indicate that electrons and $\bullet O_2^-$ are crucial in the production of H_2O_2 . As recorded in Fig. 10D, decreasing the concentration of dissolved O_2 (Ar bubbling) only limitedly reduced H_2O_2 production to 2.24 mM (30 min), and increasing the concentrations of dissolved O_2 (O_2 bubbling) increased H_2O_2 production to 6.59 mM (30 min). This yield obtained on KCN-0.5 exceeded most works that only consider obtaining more structural defects on carbon nitride ((Fig. 10E, Table S5), and with an apparent quantum yield in light utilization of 11.27%. The above results demonstrate the strong performance of KCN-0.5 in the photoreduction of O_2 to H_2O_2 , creating a prerequisite for forming a photocatalysis-self-Fenton system.

Incidentally, the reproducibility of KCN-0.5 is also satisfactory. The efficiency for photocatalytic production of H_2O_2 in the cycling experiment is almost the same as that of fresh KCN-0.5, and no crystal and surface chemical structure differences after the cycling experiment (Fig. S8).

Combined with experiments, characterization and theoretical calculations, the mechanism for constructing a photocatalysis-self-Fenton system over KCN-0.5 is illustrated in Fig. 11. Under light irradiation, KCN-0.5 generated abundant charges. Compressed π - π layer stacking ensures electrons transfer from bulk phase to surface nanoparticles. The twin structure promotes the separation of charges and limits the reverse recombination of electrons. The new N-defect with strong electrophilicity induces electrons convergence and transit to O_2 , promoting the two-electron reduction of O_2 to H_2O_2 ($O_2 + 2H^+ + 2e^- \rightarrow H_2O_2$) and further activating the H_2O_2 into hydroxyl radicals ($H_2O_2 + e^- \rightarrow \bullet OH + OH^-$). Therefore, a photocatalysis-self-Fenton system with abundant reactive species (h^+ , $\bullet O_2^-$, H_2O_2 and $\bullet OH$) constructed on the surface of KCN-0.5, which can effectively degrade and mineralize organic pollutants.

4. Conclusion

In summary, ingeniously introduced the compressed π - π layer stacking and surface-remodeled N-defect into carbon nitride through one-step thermal polymerization of urea in KCl-KOH, obtaining a defective twin carbon nitride (KCN-0.5). The performance of KCN-0.5 was far more than that of pristine carbon nitride in producing H_2O_2 and mineralizing organic pollutants. Characterization and theoretical calculation demonstrate that KCN-0.5 has excellent properties in transferring and separating charges, adsorbing and reducing O_2 . Therefore, electrons can be efficiently utilized to produce and activate H_2O_2 , constructing a photocatalysis-self-Fenton system over KCN-0.5 for mineralizing organic pollutants. This work provides a new idea for the design and synthesis of environmentally functional materials.

CRediT authorship contribution statement

Junpeng Yue: Conceptualization, Investigation, Calculation, Data curation, Writing – original draft. **Hanpei Yang:** Resources, Writing – review & editing, Supervision, Project administration, Funding acquisition. **Chen Liu:** Validation. **Qiang Zhang:** Calculation. **Yanhui Ao:** Software.

Declaration of Competing Interest

The authors declare that they have no known competing financial interests or personal relationships that could have appeared to influence

the work reported in this paper.

Data Availability

No data was used for the research described in the article.

Acknowledgments

This work was financially supported by the National Natural Science Foundation of China (Grants No. 52070070).

Appendix A. Supporting information

Supplementary data associated with this article can be found in the online version at doi:10.1016/j.apcatb.2023.122716.

References

- [1] Z.Y. Teng, Q.T. Zhang, H.B. Yang, K. Kato, W.J. Yang, Y.R. Lu, S.X. Liu, C.Y. Wang, A. Yamakata, C.L. Su, B. Liu, T. Ohno, Atomically dispersed antimony on carbon nitride for the artificial photosynthesis of hydrogen peroxide, *Nat. Catal.* 4 (2021) 374–384.
- [2] Y. Shiraishi, T. Takii, T. Hagi, S. Mori, Y. Kofuji, Y. Kitagawa, S. Tanaka, S. Ichikawa, T. Hirai, Resorcinol-formaldehyde resins as metal-free semiconductor photocatalysts for solar-to-hydrogen peroxide energy conversion, *Nat. Mater.* 18 (2019) 985–993.
- [3] Z.Z. Wang, Y.J. Zhao, Y.J. Zhou, X. Wang, H. Huang, Y. Liu, M.W. Shao, Z.H. Kang, All-in-one photocatalysis device for one-step high concentration H_2O_2 photoproduction, *Chem. Eng. J.* 427 (2022), 131972.
- [4] Y. Nosaka, A.Y. Nosaka, Generation and detection of reactive oxygen species in photocatalysis, *Chem. Rev.* 17 (2017) 11302–11336.
- [5] X.K. Zeng, Y. Liu, Y. Kang, Q.Y. Li, Y. Xia, Y.L. Zhu, H.L. Hou, M.H. Uddin, T. R. Gengenbach, D.H. Xia, C.H. Sun, D.T. McCarthy, A. Deletic, J.G. Yu, X. W. Zhang, Simultaneously tuning charge separation and oxygen reduction pathway on graphitic carbon nitride by polyethylenimine for boosted photocatalytic hydrogen peroxide production, *ACS Catal.* 10 (2020) 3697–3706.
- [6] Y. Kofuji, Y. Isobe, Y. Shiraishi, H. Sakamoto, S. Tanka, A. Ichikawa, T. Hirai, Carbon nitride-aromatic diimide-graphene nanohybrids: metal-free photocatalysts for solar-to-hydrogen peroxide energy conversion with 0.2% efficiency, *J. Am. Chem. Soc.* 138 (2016) 10019–10025.
- [7] Y. Xia, X.H. Zhao, C. Xia, Z.Y. Wu, J.Y. Kim, X.W. Bai, G.H. Gao, Y.F. Hu, J. Zhong, Y.Y. Liu, H.T. Wang, Highly active and selective oxygen reduction to H_2O_2 on boron-doped carbon for high production rates, *Nature, Communications* 12 (2021) 4225.
- [8] X.Y. Hu, X.K. Zeng, Y. Liu, J. Lu, X.W. Zhang, Carbon-based materials for photo- and electrocatalytic synthesis of hydrogen peroxide, *Nanoscale* 12 (2020) 16008–16027.
- [9] W. Liu, P. Wang, J. Chen, X. Gao, H. Che, B. Liu, Y. Ao, Unraveling the mechanism on ultrahigh efficiency photocatalytic H_2O_2 generation for dual-heteroatom incorporated polymeric carbon nitride, *Adv. Funct. Mater.* 32 (2022), 2205119.
- [10] H. Che, P. Wang, J. Chen, X. Gao, B. Liu, Y. Ao, Rational design of donor-acceptor conjugated polymers with high performance on peroxydisulfate activation for pollutants degradation, *Appl. Catal. B: Environ.* 316 (2022), 121611.
- [11] M.X. Lin, F.Y. Li, W.Y. Cheng, X.M. Rong, W. Wang, Facile preparation of a novel modified biochar-based supramolecular self-assembled g-C₃N₄ for enhanced visible light photocatalytic degradation of phenanthrene, *Chemosphere* 288 (2022), 132620.
- [12] H. Zhang, L.H. Jia, P. Wan, R.J. Xu, J. He, W. Jiang, Improved H_2O_2 photogeneration by KOH-doped g-C₃N₄ under visible light irradiation due to synergistic effect of N defects and K modification, *Appl. Surf. Sci.* 527 (2020), 146584.
- [13] R.F. Du, K. Xiao, B.Y. Li, X. Han, C.Q. Zhang, X. Wang, Y. Zou, P. Guardia, J.S. Li, J. B. Chen, J. Arbiol, A. Cabot, Controlled oxygen doping in highly dispersed Ni-loaded g-C₃N₄ nanotubes for efficient photocatalytic H_2O_2 production, *Chem. Eng. J.* 441 (2022), 135999.
- [14] X.L. Geng, L. Wang, L. Zhang, H. Wang, Y.Y. Peng, Z.Y. Bian, H_2O_2 production and in situ sterilization over a ZnO/g-C₃N₄ heterojunction photocatalyst, *Chem. Eng. J.* 420 (2021), 129722.
- [15] X.M. Dang, R.Y. Yang, Z. Wang, S.Y. Wu, H.M. Zhao, Efficient visible-light activation of molecular oxygen to produce hydrogen peroxide using P doped g-C₃N₄ hollow spheres, *J. Mater. Chem. A* 8 (2020) 22720–22727.
- [16] C. Zhao, C.J. Shi, Q. Li, X.Y. Wang, G. Zeng, S. Ye, B.J. Jiang, J. Liu, Nitrogen vacancy-rich porous carbon nitride nanosheets for efficient photocatalytic H_2O_2 production, *Mater. Today Energy* 24 (2022), 100926.
- [17] X.Y. Chang, J.J. Yang, D.D. Han, B. Zhang, X. Xiang, J. He, Enhancing light-driven production of hydrogen peroxide by anchoring Au onto C₃N₄ catalysts, *Catalysts* 8 (2018).
- [18] Y.K. Wang, S.Z. Hu, Q. Li, G.Z. Gu, Y.F. Zhao, H.Y. Liang, W. Li, One step synthesis of high-efficiency AgBr-Br-g-C₃N₄ composite catalysts for photocatalytic H_2O_2 production via two channel pathway, *RSC Adv.* 8 (2018) 36903–36909.

- [19] Y. Zhao, L. Wang, R. Malpass-Evans, N.B. Mckeown, M. Carta, J.P. Lowe, C.L. Lyall, R. Castaing, P.J. Fletcher, G. Kociok-Kohn, J. Wenk, Z.Y. Guo, F. Marken, Effects of g-C₃N₄ heterogenization into intrinsically microporous polymers on the photocatalytic generation of hydrogen peroxide, *ACS Appl. Mater. Interfaces* 14 (2022) 19938–19948.
- [20] H.H. Zhu, Q. Xue, G.Y. Zhu, Y. Liu, X.Y. Dou, X. Yuan, Decorating Pt@cyclodextrin nanoclusters on C₃N₄/MXene for boosting the photocatalytic H₂O₂ production, *J. Mater. Chem. A* 9 (2021) 6872–6880.
- [21] J. Tan, N. Tian, Z.F. Li, X.L. Yao, M. Vakili, Y. Lu, T.T. Zhang, Intrinsic defect engineering in graphitic carbon nitride for photocatalytic environmental purification: a review to fill existing knowledge gaps, *Chem. Eng. J.* 421 (2021), 127729.
- [22] X.N. Yu, S.F. Ng, L.K. Putri, L.L. Tan, A.R. Mohamed, W.J. Ong, Point-defect engineering: leveraging imperfections in graphitic carbon nitride (g-C₃N₄) photocatalysts toward artificial photosynthesis, *Small* 17 (2021), 2006851.
- [23] B.Y. Liu, J.Y. Du, G.L. Ke, Y.J. Huang, H.C. He, Y. Zhou, Z.G. Zou, Boosting O₂ reduction and H₂O dehydrogenation kinetics: surface N-hydroxymethylation of g-C₃N₄ photocatalysts for the efficient production of H₂O₂, *Adv. Funct. Mater.* 32 (2021), 2111125.
- [24] S. Wu, H.T. Yu, S. Chen, X. Quan, Enhanced photocatalytic H₂O₂ production over carbon nitride by doping and defect engineering, *ACS Catal.* 10 (2020) 14380–14389.
- [25] Z. Wei, M.L. Liu, Z.J. Zhang, W.Q. Yao, H.W. Tan, Y.F. Zhu, Efficient visible-light-driven selective oxygen reduction to hydrogen peroxide by oxygen-enriched graphitic carbon nitride polymers, *Energy Environ. Sci.* 11 (2018) 2581–2589.
- [26] L. Zhou, J.Y. Lei, F.C. Wang, L.Z. Wang, M.R. Hoffmann, Y.D. Liu, S.L. In, J. L. Zhang, Carbon nitride nanotubes with in situ grafted hydroxyl groups for highly efficient spontaneous H₂O₂ production, *Appl. Catal. B: Environ.* 288 (2021), 119993.
- [27] C.Y. Feng, L. Tang, Y.C. Deng, J.J. Wang, J. Luo, Y.N. Liu, X.L. Ouyang, H.R. Yang, J.F. Yu, J.J. Wang, Synthesis of Leaf-Vein-Like g-C₃N₄ with tunable band structures and charge transfer properties for selective photocatalytic H₂O₂ Evolution, *Adv. Funct. Mater.* 30 (2020), 2001922.
- [28] J.Y. Lei, V. Chen, W.J. Lv, L. Zhou, L.Z. Wang, Y.D. Liu, J.L. Zhang, Robust photocatalytic H₂O₂ production over inverse Opal g-C₃N₄ with carbon vacancy under visible light, *ACS Sustain. Chem. Eng.* 7 (2019) 16467–16473.
- [29] L. Shi, L.Q. Yang, W. Zhou, Y.Y. Liu, L.S. Yin, X. Hai, H. Song, J.H. Ye, Photoassisted construction of holey defective g-C₃N₄ photocatalysts for efficient visible-light-driven H₂O₂ production, *Small* 14 (2018), 1703142.
- [30] H.L. Hou, X.K. Zeng, X.W. Zhang, Production of hydrogen peroxide by photocatalytic processes, *Angew. Chem. Int. Ed. Engl.* 59 (2020) 17356–17376.
- [31] Y.D. Wang, D. Meng, X. Zhao, Visible-light-driven H₂O₂ production from O₂ reduction with nitrogen vacancy-rich and porous graphitic carbon nitride, *Appl. Catal. B: Environ.* 273 (2020), 119064.
- [32] J. Yang, Y.J. Liang, K. Li, G. Yang, K. Wang, R. Xu, X.J. Xie, One-step synthesis of novel K⁺ and cyano groups decorated triazine/heptazine-based g-C₃N₄ tubular homojunctions for boosting photocatalytic H₂ evolution, *Appl. Catal. B: Environ.* 262 (2020), 118252.
- [33] H.J. Yu, R. Shi, Y.X. Zhao, Y.F. Zhao, C. Zhou, C.I.N. Waterhouse, L.Z. Wu, C. H. Tung, T.R. Zhang, Alkali-assisted synthesis of nitrogen deficient graphitic carbon nitride with tunable band structures for efficient visible-light-driven hydrogen evolution, *Adv. Mater.* 29 (2017), 1605148.
- [34] J. Colina-Marquez, F. Machuca-Matinez, G.Li Puma, Radiation absorption and optimization of solar photocatalytic reactors for environmental applications, *Environ. Sci. Technol.* 44 (2010) 5112–5120.
- [35] D. Dolat, N. Quici, E. Kusiak-Nejman, A.W. Morawski, G.Li Puma, One-step, hydrothermal synthesis of nitrogen, carbon co-doped titanium dioxide (N,C-TiO₂) photocatalysts. Effect of alcohol degree and chain length as carbon dopant precursors on photocatalytic activity and catalyst deactivation, *Appl. Catal. B: Environ.* 115–116 (2012) 81–89.
- [36] J. Xiong, X.B. Li, J.T. Huang, X.M. Gao, Z. Chen, J.Y. Liu, H. Li, B.B. Kang, W. Q. Yao, Y.F. Zhu, CN/rGO@BPQDs high-low junctions with stretching spatial charge separation ability for photocatalytic degradation and H₂O₂ production, *Appl. Catal. B: Environ.* 266 (2020), 118602.
- [37] G. Li Puma, A. Brucato, Dimensionless analysis of slurry photocatalytic reactors using two-flux and six-flux radiation absorption–scattering models, *Catal. Today* 122 (2007) 78–90.
- [38] G.G. Zhang, G.S. Li, Z.A. Lan, L.H. Lin, A. Savateev, T. Heil, S. Zafeiratos, X. C. Wang, M. Antonietti, Optimizing optical absorption, exciton dissociation, and charge transfer of a polymeric carbon nitride with ultrahigh solar hydrogen production activity, *Angew. Chem. Int. Ed. Engl.* 56 (2017) 13445–13449.
- [39] Y.F. Chen, X.M. Yan, J.X. Xu, L. Wang, K⁺, Ni and carbon co-modification promoted two-electron O₂ reduction for photocatalytic H₂O₂ production by crystalline carbon nitride, *J. Mater. Chem. A* 9 (2021) 24056–24063.
- [40] P.F. Xia, M. Antonietti, B.C. Zhu, T. Heil, J.G. Yu, S.W. Cao, Designing defective crystalline carbon nitride to enable selective CO₂ photoreduction in the gas phase, *Adv. Funct. Mater.* (2019), 1900093.
- [41] S. Bai, N. Zhang, C. Gao, Y.J. Xiong, Defect engineering in photocatalytic materials, *Nano Energy* 53 (2018) 296–336.
- [42] L. Chen, D.Y. Zhu, J.T. Li, X.X. Wang, J.F. Zhu, P.S. Francis, Y.H. Zheng, Sulfur and potassium co-doped graphitic carbon nitride for highly enhanced photocatalytic hydrogen evolution, *Appl. Catal. B: Environ.* 273 (2020), 119050.
- [43] Z.H. Liao, C.X. Li, Z. Shu, J. Zhou, T.T. Li, W.B. Wang, Z.L. Zhao, L.N. Xu, L.L. Shi, L.L. Feng, K–Na co-doping in crystalline polymeric carbon nitride for highly improved photocatalytic hydrogen evolution, *Int. J. Hydrog. Energy* 46 (2021) 26318–26328.
- [44] Q. Zhang, J. Chen, X. Gao, H.N. Che, P.F. Wang, Y.H. Ao, In-depth insight into the mechanism on photocatalytic synergistic removal of antibiotics and Cr (VI): The decisive effect of antibiotic molecular structure, *Appl. Catal. B: Environ.* 15 (2022), 121443.
- [45] J.R. Ran, T.Y. Ma, G.P. Gao, X.W. Du, S.Z. Qiao, Porous P-doped graphitic carbon nitride nanosheets for synergistically enhanced visible-light photocatalytic H₂ production, *Energy Environ. Sci.* 8 (2015) 3708–3717.
- [46] X. Zhang, P.J. Ma, C. Wang, L.Y. Gan, X.J. Chen, P. Zhang, Y. Wang, H. Li, L. H. Wang, X.Y. Zhou, K. Zheng, Unraveling the dual defect sites in graphitic carbon nitride for ultra-high photocatalytic H₂O₂ evolution, *Energy Environ. Sci.* 15 (2022) 830–842.
- [47] A. Kumar, P. Raizada, A. Hosseini-Bandegharai, V.K. Thakur, V. Nguyen, P. Singh, C-, N-Vacancy defect engineered polymeric carbon nitride towards photocatalysis: viewpoints and challenges, *J. Mater. Chem. A* 9 (2021) 111–153.
- [48] G.Q. Zhang, Y.S. Xu, M. Rauf, J.Y. Zhu, Y.L. Li, C.X. He, X.Z. Ren, P.X. Zhang, H. W. Mi, Breaking the limitation of elevated coulomb interaction in crystalline carbon nitride for visible and near-infrared light photoactivity, *Adv. Sci.* 9 (2022), 2201677.
- [49] Y.Y. Duan, Y. Wang, L.Y. Gan, J.Z. Meng, Y.J. Feng, K.W. Wang, K. Zhou, C. Wang, X.D. Han, X.Y. Zhou, Amorphous carbon nitride with three coordinate nitrogen (N_{3c}) vacancies for exceptional NO_x abatement in visible light, *Adv. Energy Mater.* 11 (2021), 2004001.
- [50] L.H. Lin, W. Ren, C. Wang, A.M. Asiri, J. Zhang, X.C. Wang, Crystalline carbon nitride semiconductors prepared at different temperatures for photocatalytic hydrogen production, *Appl. Catal. B: Environ.* 231 (2018) 234–241.
- [51] L.T. Ma, H.Q. Fan, K. Fu, S.H. Lei, Q.Z. Hu, H.T. Huang, G.P. He, Protonation of graphitic carbon nitride (g-C₃N₄) for an electrostatically self-assembling carbon@g-C₃N₄ core-shell nanostructure toward high hydrogen evolution, *ACS Sustain. Chem. Eng.* 5 (2017) 7093–7103.
- [52] Q. Zhang, J. Chen, X. Gao, H.N. Che, Y.H. Ao, P.F. Wang, Understanding the mechanism of interfacial interaction enhancing photodegradation rate of pollutants at molecular level: Intermolecular π - π interactions favor electrons delivery, *J. Hazard. Mater.* 15 (2022), 128386.
- [53] P. Niu, M. Qiao, Y.F. Li, L. Huang, T.Y. Zhai, Distinctive defects engineering in graphitic carbon nitride for greatly extended visible light photocatalytic hydrogen evolution, *Nano Energy* 44 (2018) 73–81.
- [54] Y.W. Li, Z.F. Zhang, S.Z. Li, L.Y. Liu, W.L. Ma, Solar-induced efficient propylparaben photodegradation by nitrogen vacancy engineered reticulate g-C₃N₄: Morphology, activity and mechanism, *Sci. Total Environ.* 856 (2023), 159247.
- [55] G.Q. Zhang, Y.S. Xu, D.F. Yan, C.X. He, Y.L. Li, X.Z. Ren, P.X. Zhang, H.W. Mi, Construction of K⁺ ion gradient in crystalline carbon nitride to accelerate exciton dissociation and charge separation for visible light H₂ production, *ACS Catal.* 11 (2021) 6995–7005.
- [56] H.H. Liu, D.L. Chen, Z.Q. Wang, H.J. Jing, R. Zhang, Microwave-assisted molten-salt rapid synthesis of isotype triazine/heptazine based g-C₃N₄ heterojunctions with highly enhanced photocatalytic hydrogen evolution performance, *Appl. Catal. B: Environ.* 203 (2017) 300–313.
- [57] S.C. Wang, Y.L. Li, X. Wang, G.H. Zi, C.Y. Zhou, B.Y. Liu, G. Liu, L.Z. Wang, W. Huang, One-step supramolecular preorganization constructed crinkly graphitic carbon nitride nanosheets with enhanced photocatalytic activity, *J. Mater. Sci. Technol.* 104 (2022) 155–162.
- [58] G.G. Zhang, A. Savateev, Y.B. Zhao, L.N. Li, M. Antonietti, Advancing the $n \rightarrow \pi^*$ electron transition of carbon nitride nanotubes for H₂ photosynthesis, *J. Mater. Chem. A* 5 (2017) 12723.
- [59] T. Xiong, W.L. Cen, Y.X. Zhang, F. Dong, Bridging the g-C₃N₄ interlayers for enhanced photocatalysis, *ACS Catal.* 6 (2016) 2462–2472.
- [60] H.N. Che, X. Gao, J. Chen, J. Hou, Y.H. Ao, P.F. Wang, Iodide-induced fragmentation of polymerized hydrophilic carbon nitride for high-performance quasi-homogeneous photocatalytic H₂O₂ production, *Angew. Chem. Int. Ed.* 60 (2021) 25546–25550.